In-Situ Mechanical Property Measurement and Influence of Impurity Elements on Grain Boundary Strength of Cr and Mo Alloys

B. S.-J. Kang[1], C.-Y. Feng[1], A. Manivannan[2], N. Ma[2], and B.R. Cooper[2]
[1]Mechanical and Aerospace Engineering Department
[2]Physics Department
West Virginia University
Morgantown, WV 26506

ABSTRACT

This research is (i) to conduct atomistic computational modeling and simulations on the influence of carbon and oxygen to grain boundary strength and interfacial fracture of molybdenum alloys, and (ii) to apply and further develop of a transparent indenter measurement (TIM) method for in-situ material mechanical property measurement of selected metallic alloys relevant to the Fossil Energy Materials Program**.** Impurity elements segregated near the grain boundaries such as O, N and S can have important effects on the mechanical properties of hosting structural materials. To minimize the detrimental effects, dispersions (MgO for Cr) or other impurities (C for Mo) are included to alter the microstructures, sometimes resulting in improved ductility. However, the fundamental mechanism is not clear, and the relationship between the features in the microstructure and the ductility enhancement is not robust. A more fundamental mechanism at the atomic scale will provide insightful information. Using FP-LMTO techniques, a number of numerical simulations were carried out to probe the changes in electronic structures and chemical bonding properties due to the complex interactions among the impurity elements and the hosting metal or metal-oxide interface. Interesting features in the charge density distribution plot were noted, which may link to ductility enhancement. Such correlations can help to better understand the mechanism and predict the optimal composition for additives. For the second task, an in-situ TIM method was developed for material mechanical property evaluation based on spherical indentation. During indentation process, the in-situ measurement of out-of-plane deformation was carried out using integrated phase-shifting Twyman-Green interferometer. Based on elastic recovery theories and 2D finite element analyses, a procedure was developed to determine the material Young's modulus using the measured out-of-plane deformation. During loading, the contact radius of spherical indentation was continuously measured and used to estimate the material post-yielding true stress-strain curve using Tabor's empirical relation. Preliminary tests were conducted on several engineering materials and the results showed good agreement with known material properties.

INTRODUCTION

A number of molybdenum-based structural materials are currently being developed for ultra-high temperature (>1000°C) applications beyond those presently attainable with nickel-based

super-alloys[1-9]. These materials consist of thermodynamically stable three-phase mixtures of Mo, Mo_3Si and Mo_5SiB_2, and possess attractive combination of high melting point (around 2000°C), good high-temperature oxidation resistance and excellent corrosion resistance in many environments, which makes them of great interest for fossil energy applications.

Segregated near the grain boundaries, impurity elements such as O, N and S, can have important effects on the mechanical properties of hosting structural materials. To minimize the detrimental effects, dispersions (MgO for Cr) or other impurities (C for Mo) are included to alter the microstructures, sometimes resulting in improved ductility. However, the fundamental mechanism is not clear, and the relationship between the features in the microstructure and the ductility enhancement is not robust. For example, although the inclusion of TiO_2 and La_2O_3 dispersions in Cr displays similar microstructure patterns as does MgO, the ductility is not correspondingly improved. We therefore believe a more fundamental mechanism at the atomic scale will provide insightful information. In this research, we first conducted atomistic computational modeling and simulations on the influence of carbon and oxygen to grain boundary strength and interfacial fracture of molybdenum alloys. Using FP-LMTO techniques, we first carried out a number of numerical simulations to probe the changes in electronic structures and chemical bonding properties due to the complex interactions among the impurity elements and the hosting metal or metal-oxide interface. For the second task, an in-situ transparent indenter measurement (TIM) method was developed for material mechanical property evaluation based on spherical indentation technique. Our goal is to apply and further develop of the TIM method for in-situ material mechanical property measurement as well as quick assessment of brittleness/ductility of alloys relevant to the Fossil Energy Materials Program**.**

Task 1: Atomistic Modeling and Simulation

1.1 Oxygen impurity effects on molybdenum grain boundary

In order to ensure maximum ductility of molybdenum phase it is desirable to inhibit intergranular fracture. Experimental evidence has correlated the intergranular fracture of Mo with the presence of oxygen impurities segregated in the vicinity of Mo grain boundary. It is well known that the grain boundary segregation of impurity elements like oxygen and others can strongly affects the mechanical

properties of structural materials, but the detailed fundamental mechanisms depend on specific impurity elements and the hosting material.

To understand these mechanisms, we carried out atomistic simulations using full potential linear muffin tin orbital (FP-LMTO) techniques [10-11]. The supercell of the simulated system consists of six molybdenum atoms and two oxygen atoms (Figure 1a). The molybdenum atoms were initially put on a body centered cubic (b.c.c.) lattice, while the two oxygen atoms were then introduced as interstitial impurities at the octahedral centers. As the supercell repeats itself to fill up the space, the oxygen impurities will actually form a double layer, representing an idealized case of segregation near the molybdenum grain boundary. The atoms were then allowed to relax their position to minimize the total energy of the system.

After equilibrium was reached, we calculated the charge distribution of the system. Figure 1b shows the contour plot of the calculated charge distribution on Mo's (1,1,0) cross section plane. Note that the superpositioned charge distribution of the corresponding free atom species has been subtracted, i.e.,

$$\tilde{\rho}(R) = \rho(R) - \sum_i \rho^0(R - R_i),$$

where, ρ^0 is the charge density of a corresponding free atom, ρ and $\tilde{\rho}$ are the calculated and plotted charge density, respectively. For convenience, we will call $\tilde{\rho}$ "bonding charge density". Therefore, the red (or blue) area in the plot indicates a region where the electron charge density has increased (or decreased) due to the formation of solid. For comparison, the similarly prepared bonding charge contour plot of a pure b.c.c. Mo system is displayed in Figure 1c.

Apart from the apparent lattice relaxation (which clearly indicates a stretch and weakening of Mo bonds), we see a number of changes in the electronic structure features:

(1) The oxygen core area is marked red since it withdraws charges from surrounding and other areas and becomes ionized. In response, the surrounding areas try to screen the extra charges in the core by forming a blue shell with decreased electron density.

(2) The ionic oxygen induces severe charge density fluctuations among the adjacent Mo atoms. For the immediate neighboring Mo atom (denoted by Mo^1), even in the core area, charge distribution is being significantly altered compared with the pure Mo atom (displayed on right panel): more blue areas appear, meaning that some core electrons have leaked out to the surrounding electron clouds, thus making Mo^1 partially ionized. The partially ionized Mo^1 then forms strong ionic bonds with the ionic oxygen.

(3) When we looked at the second nearest Mo atom (denoted by Mo^2), it is not as partially ionized as the Mo^1. However, affected by the presence of the nearby oxygen, there is a net increase of charge in their surrounding electron clouds. This induced charge must have come from other regions of the system, i.e., from nearby third layer Mo (denoted by Mo^3), or from interstitial free electrons that are responsible for the metallic bonding. In either case, since electrons are asymmetrically localized (as being captured by the Mo^2 core), the Mo^2-Mo^3 bond is weakened.

Overall, we have seen that the introduction of oxygen impurity has induced significant electronic charge redistribution in its nearby regions. Some interstitial free electrons originally responsible for Mo-Mo metallic bonding are either withdrawn by oxygen to form ionic bonds, or swallowed by the first or second layer Mo's electron clouds to become more localized. Therefore, the characteristic of bonding changes from metallic to partial ionic. Since the original metallic bonds are crucial to hold the solid flexible upon deformation and to resist cracking, we conclude that the mechanical property is compromised, i.e. trace amount of residual oxygen at grain boundary promotes intergranular fracture. The fracture is most likely mediated through broken bonds between the second and third layer Mo, since the chemical bonding is significantly weakened there as indicated in our simulation.

This helps to explain the experimental observations. We see the unalloyed Mo with grain boundary oxygen impurities suffers from low fracture toughness. The observed failure type is mostly intergrannular fracture. When Si and B are included in the alloy system, they tend to form protective silica glass scale to prevent further oxidation [1-9]. Therefore, depending on the microstructural morphology, the grain boundary oxygen impurity level will decrease, yielding a much tougher Mo phase.

However, as the applied load ultimately exceeds the strength of Mo_3Si and Mo_5Si_2B, catastrophic failure (i.e. transgrannular fracture) occurs due to the brittleness of the ceramic phases.

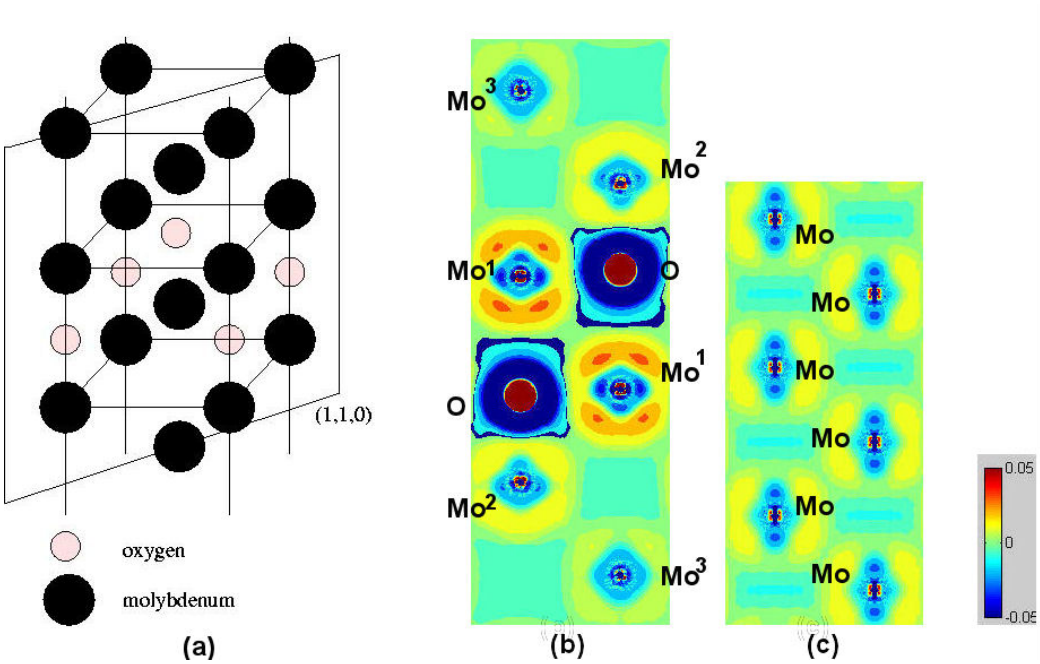

Figure 1. (a) the unit cell of simulated Mo system with oxygen impurities, (b) bonding charge density contour plot, and (c) bonding charge density contour plot for a pure Mo system. The colorbar scale is in unit of $bohr^{-2}$.

1.2 The inclusion of MgO to control nitrogen impurities effects in chromium

Having seen the detrimental effects of segregated impurities, we seek for solutions to counteract the impurity effects, or at least to control the damage. The inclusion of metal oxide dispersions has proven to provide an effective way to manipulate the impurity segregation at grain boundaries. In a recent experiment, Brady and coworkers [12] has demonstrated nicely that tiny dispersions of MgO can improve the ductility of Cr. Through microstructural analysis, they found nitrogen impurities appears to be mostly segregated to the vicinity of oxide-metal interface. Therefore, they hypotheses that the MgO phase tends to attract nitrogen impurities and thus prevents them from segregating to the Cr grain boundaries and forming brittle nitrides.

To understand the fundamental mechanism responsible for the ductility enhancement, we performed a comparative study about the MgO effects on Cr with N impurities. Shown in Figures 2a and 3a are system I and II we have studied, respectively. Both systems consist of four Cr, two N, two Mg,

and two O atoms. The difference is that in system I, the N atoms are placed at the center between the 4 Cr layers (notice the periodic boundary conditions imposed in z-direction), whereas in system II, they are placed in between the Cr-MgO interface. Therefore, system I represents a Cr-MgO system with N impurities segregated at the Cr grain boundary, whereas system II represents a system with impurities attracted by MgO and thus a clean Cr grain boundary. Both systems were relaxed from their initial configuration, until an equilibrium configuration is reached.

At equilibrium, system I is 18eV/atom less stable than system II. This shows that nitrogen impurities are stabilized by MgO-Cr interface, supporting the impurity management conclusion from experiment. Figures 2b and 3b show the corresponding bonding charge density contour plot at equilibrium. Comparing the two systems, we found the following common features:

(1) In both cases, the nitrogen core is marked red and surrounded by a blue shell: just like the case of oxygen in molybdenum, nitrogen will withdraw some charges from other atoms and becomes ionized, and the blue shell comes from the induced screening effects.

(2) Interestingly, the oxygen atoms, whose cores are also marked red, are not surrounded by blue shells. The electric field due to their excessive charge must have been screened very well by the nearby Mg ions, and thus no additional interstitial screening is necessary.

(3) In both cases, the charge density distribution near Cr atoms is significantly altered. More localized charge around Cr, and less interstitial charge to form metallic bonds.

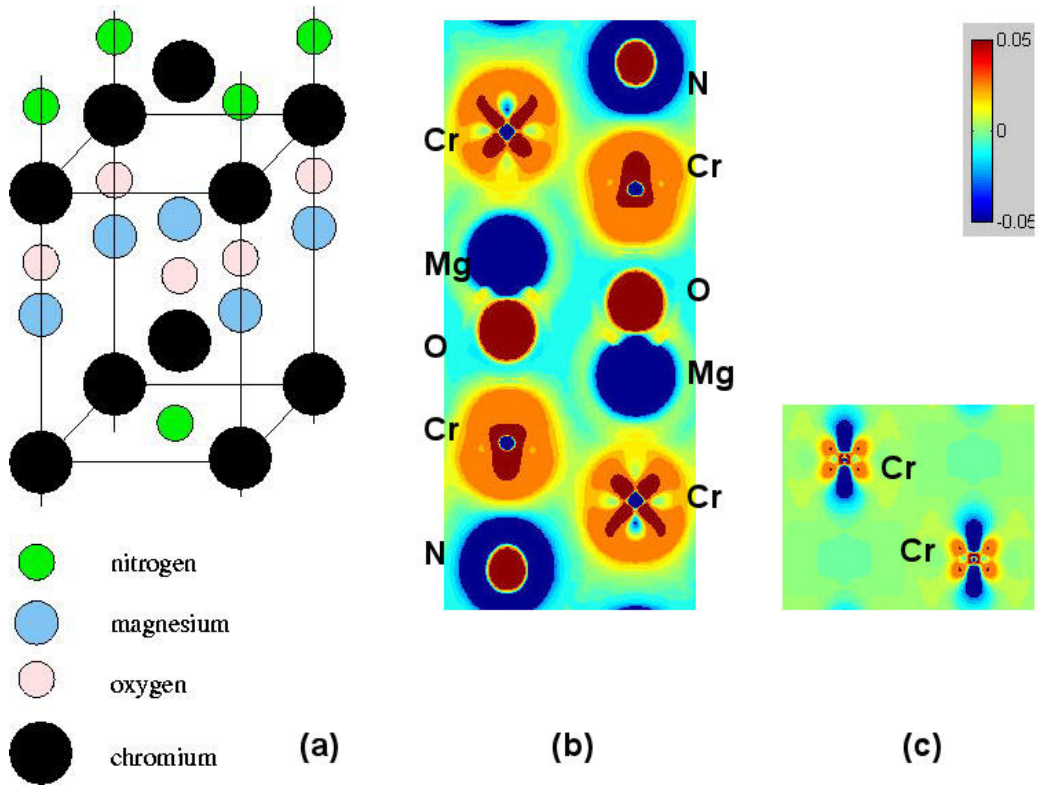

Figure 2. (a) the unit cell of simulated MgO-Cr system with nitrogen impurities at the Cr boundary, (b) bonding charge density contour plot, and (c) bonding charge density contour plot for a pure Cr system. The colorbar scale is in unit of bohr^{-2}.

However, with nitrogen placed near the MgO-Cr interfacial boundary, system II displays some important new features:

(1) The nitrogen ion's excessive charge is partially screened by the nearby Mg atom. This is reflected by the fact that the blue areas overlap in Figure 3b.

(2) Because of Mg's partial screening, the detrimental effects due to nitrogen are not as severe as in system I. For example, the charge distribution near the Cr atoms is mildly red in system II. The charge density in the interstitial area is also a little bit higher (green as compared to blue) than system I, indicating better metallic bonding.

(3) Also if we look at the Mg-O ionic bonding, due to the Mg's partial screening for ionic nitrogen, the screening of ionic oxygen is less perfect, as manifested by a light blue shell around oxygen core. This indicates that the Mg-O ionic bond is weakened.

In summary, we found that the Mg ion in MgO will stabilize a nearby negatively charged nitrogen impurity by providing partial screening, therefore neutralizing the detrimental effects of nitrogen on Cr-Cr metallic bonds. This conclusion is in agreement with the experiment. Essentially, the detrimental impurities create charge redistribution and change the nature of the chemical bonding from metallic to partially ionic. The inclusion of MgO counteracts the above effects by protecting the metallic bonds. It does so at the cost of weakened Mg-O ionic bonds.

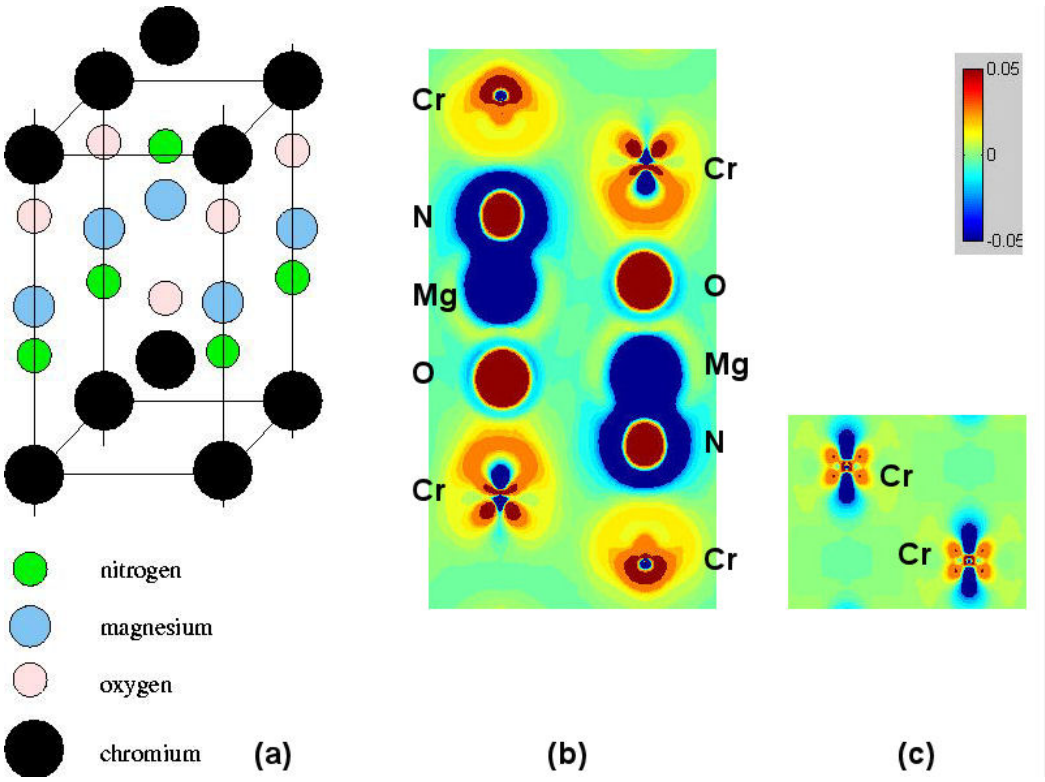

Figure 3. (a) the unit cell of simulated MgO-Cr system with nitrogen impurities near the interface, (b) bonding charge density contour plot, and (c) bonding charge density contour plot for a pure Cr system. The colorbar scale is in unit of bohr^{-2}.

1.3 The effects of the inclusion of TiO_2

An interesting discovery of Brady's experiment is that the ductility enhancement by metal oxide dispersion appears to be unique. Some other types of metal oxides, including TiO_2, La_2O_3, and ZrO_2, have been used in replacement for MgO to investigate the ductility enhancement mechanism. Although microstructural analysis has revealed similar impurity stabilization effects by these oxides (i.e., the impurity will tend to segregate near the oxide-Cr interface), none has displayed the corresponding dustily

enhancement. In some case the sample even became brittle. Therefore, mechanisms based solely on microstructual analysis, such as the grain boundary impurity management, are not adequate to explain the ductility enhancement. Here, we attempt to solve the problem base on an electronic structural point of view.

As in the case of MgO, we set up a model system of TiO_2-Cr-N as shown in Figure 4a. Since we are not going to reinvestigate the impurity stabilization mechanism, we place the N directly near the interface of TiO_2 and Cr.

At equilibrium, the bonding charge density is plotted in Figure 4b. There are a number of clear differences compared the case of MgO in Figure 3b:

(1) The ionic nitrogen charge does not seem to be screened by Ti. In fact, the nitrogen goes closer to the Cr side rather than sticking with Ti. (Note the system starts with N placed at the center line between Cr and TiO_2). Therefore, its detrimental effects are not alleviated by the inclusion of TiO_2.

(2) In addition, the oxygen atom now is surrounded by a screening blue shell. Such blue shell was not present in the Cr-MgO system. This clearly demonstrates that Ti, unlike Mg, lacks the capability of helping to screen ionic oxygen or nitrogen nearby. This capability has been found crucial to explain the stabilization for charged impurities and the alleviation of their detrimental effects.

(3) As expected, the charge redistribution of nearby Cr is much more significant compared to the MgO case, due to the combined detrimental effects of both oxygen and nitrogen.

In closing, we found the ionic Ti does not possess the capability to screen nearby negatively charged ions. In consequence, the detrimental effects of both oxygen and nitrogen combined to undermine Cr metallic bonds. This may help to explain the none-ductility enhancement results seen in the experiment.

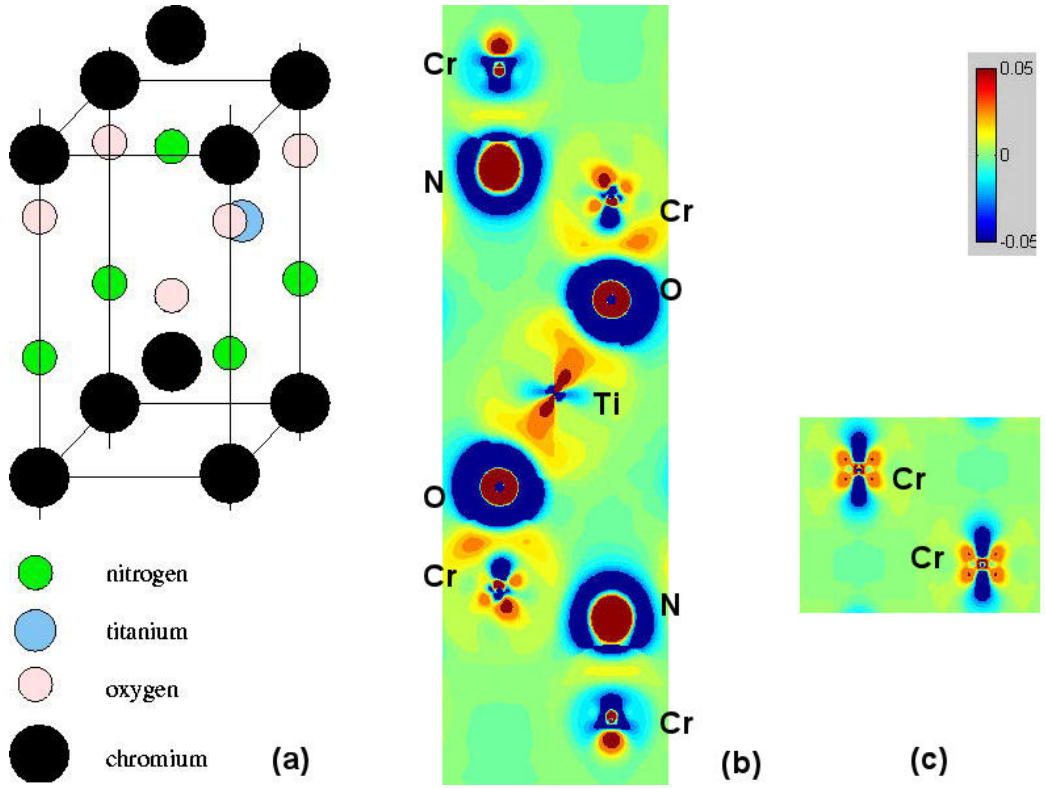

Figure 4. (a) the unit cell of simulated TiO_2-Cr system with nitrogen impurities near the interface, (b) bonding charge density contour plot, and (c) bonding charge density contour plot for a pure Cr system. The colorbar scale is in unit of $bohr^{-2}$.

1.4 Discussions

Recent experimental evidence shows clearly that carbon additions to molybdenum can effectively reduce oxygen segregation at the grain boundaries and counteract intergranular fracture. It would be important to know to what extent the strength of molybdenum grain boundaries is influenced by segregation of carbon and oxygen. Significant calculations on this topic do not appear to have been made to date. In addition, there may also be other trace additions which may, or may not, have a beneficial effect on grain boundary strength.

Further theoretical investigation is needed to study various impurity (in particular oxygen and carbon) grain boundaries segregation effects on the mechanical properties of molybdenum, and identify those that may help to improve the intergranular fracture resistance of molybdenum. The future research will emphasize on an understanding of the fundamental mechanism at the atomic and electronic structure level, which will complement experimental result based on microstructural analysis at the micron-scale

level. Since the mechanism behind many of the beneficial/detrimental effects by impurity additions can only be adequately understood from the electronic structure and chemical bonding differences among different chemical species, which is currently beyond the experimental scope, the proposed theoretical work therefore serves an indispensable means to provide insightful knowledge and useful guideline for proper additions for improved and robust ductility enhancement effects.

1.5 Overview of methodology

Most of our work performed so far was based on first principle, quantum mechanical, full potential linear muffin tin orbital techniques (FP-LMTO) [10-11]. Based on the density functional theory (DFT), FP-LMTO is among the most accurate and reliable first-principles methods currently available. It is especially suitable for the modeling of transitional metal such as Mo, where the localized and complicated nature of *d* orbital may cause problem for other plain-wave based methods.

In addition, we have also developed a unique scheme to integrate the ab-initio FP-LMTO and semi-empirical tight-binding (TB) schemes into one powerful multi-scale modeling tool to combine the accuracy and efficiency provided by each method. With the efficiency provided by TB method, our modeling capability is boosted to 10^5 atom system size, capable of typical nano-scale simulations.

Task 2: In-situ Indentation TIM Method

In this research task, we introduce a new experimental technique, Transparent Indenter Measurement (TIM) method recently developed at WVU. During indentation process, in-situ measurement of out-of-plane deformation was carried out using phase-shifting Twyman-Green interferometry. Based on elastic recovery theories and 2D finite element simulation, a procedure was developed to determine the material Young's modulus using measured out-of-plane deformation. The featured transparent indenter design also allowed real-time direct measurement of contact radius which was then used to estimate post-yielding true stress-strain data based on Tabor's empirical relation [13]. The TIM method can also be applied to assess the state of brittleness/ductility of the sample alloys. Only small piece of alloy is needed for the TIM indentation tests, which should be very convenient for alloy development. It is our intention to further development and apply the TIM method for relevant alloys

development under the Fossil Energy Materials Program. The following is an introduction of the TIM method with preliminary tests.

2.1 Elastic recovery of indentation unloading process

Since indentation unloading is an elastic process, the elastic solution is applied to characterize the unloading process. For indentations on pure elastic materials, both flat-end punch and spherical indentation solutions are available. For spherical indentation [14],

$$u_z(\rho,0) = \frac{3}{4}\frac{1-v^2}{E}\frac{P}{\pi a^3}\left[\left(2a^2-\rho^2\right)\sin^{-1}\left(\frac{a}{\rho}\right)+a\sqrt{\rho^2-a^2}\right], \quad \rho > \mathrm{a} \qquad (1)$$

Where a is the contact radius and is the distance to the indentation center.

For an indentation test, the distribution of unloading-induced elastic recovery of indentation (Δw) can be modeled by Eq.(1) for spherical indentation, where Poisson's ratio and Young's modulus are the only mechanical properties involved. Thus Young's modulus can be determined from Eq. (1) if Poisson's ratio is known [15].

2.2 Finite element analysis

Finite element analyses were conducted to investigate the indentation elastic recovery and develop the procedure for Young's modulus calculation. Elastic-plastic material model was used to study the effects of material non-linearity and deformation on the elastic recovery. A 8mm×8mm axisymmetric 2D model with 2mm diameter indenter was used in the simulation. General purpose finite element software package ABAQUS™ was chosen to carry out all simulations. Both rigid and deformable indenters were considered to study the effects of indenter rigidity on the elastic recovery. The FEA mesh consists of 6481 axisymmetric four-node linear quadrilateral elements and reduced integration was adopted. Table 1 shows the material matrix used in the simulations.

Table 1 Material matrix for FEA

Specimen(IN783[16])	Indenter (BK7 optical glass)
E=177.3GPa σ_y=779MPa σ_{ult}=1194MPa (20%strain) υ=0.31	Rigid indenter Deformable indenter E=81GPa υ =0.206

2.3. EXPERIMENTAL

2.3.1 TIM System

Figure 5 shows the optical principle of the TIM system of which Twyman-Green interferometer and spherical indentation are integrated together. As shown, a 2mm diameter transparent indenter is attached to a non-polarizing cubic beam splitter. The two stacked cubic beam splitters are used to transfer load, incident light and capture images during indentation process.

The integrated Twyman-Green interferometer [17] can be used to directly measure the indentation-induced out-of-plane deformation. By introducing phase shifting technique, the measurement spatial resolution is further enhanced. As shown in Figure 5, the beam incident to the specimen has the polarization direction perpendicular to the paper and is reflected back to the imaging system without changing polarization direction. The reference beam passes through a quarter waveplate twice, thus the polarization direction is changed 90 degree. These two beams are now mutually perpendicular. Phase shifting is introduced as these two mutually perpendicular beams entering the liquid crystal variable retarder (LCVR). A polarizer is used to view the fringe pattern in the imaging system [17]. For a BK7 indenter with a HeNe laser (632.8nm wavelength), each fringe pattern represents 208.6nm out-of-plane deformation.

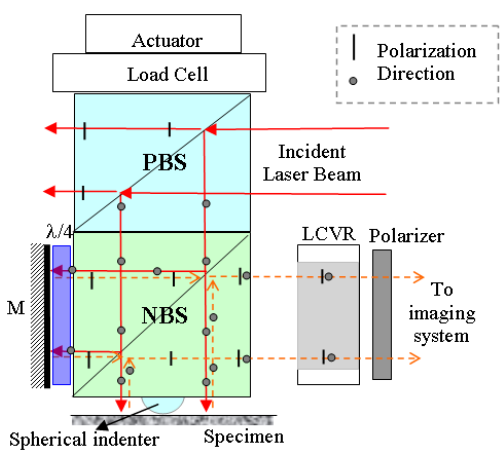

PBS: Polarization cubic beam-splitter, **NBS**: Non-polarization cubic beam-splitter,
LCVR: Liquid crystal variable retarder, **M**: Reference mirror, ***λ/4***: quarter waveplate

Figure 5. Optical principle of the Through Indenter Measurement (TIM) system

2.3.2 Test Procedures

A typical TIM test involves two loading-unloading procedures at the same indentation spot. The first loading-unloading is aimed to measure the Young's modulus, and the second is aimed to establish the post-yielding stress-strain data.

At the first loading-unloading procedure, a small load is applied and the real-time out-of-plane deformation is measured. Then the load is released and the corresponding residual out-of-plane deformation is measured. From the out-of-plane displacements, Young's modulus is calculated using Eq.1. After the first loading-unloading procedure, a sequence of monotonically increasing loads is applied at the same indented location. Here the measurement is focused on the post-yielding stress-strain data. Using TIM method, contact radius and the applied loads are measured incrementally to obtain sufficient data which are then used to establish the post-yielding stress-strain data using Tabor's empirical relation [13].

2.3.3 Test Alloys

For validity of the TIM method, experiments were done on two materials, IN783 and Al6061-T0 alloys. Initial residual stress is negligible in both of the materials. The IN783 superalloy had standard heat treatment (1120°C/1hr/AC+845°C/8hrs/AC+720°C/8hrs 50°C/hr 620°C/8hrs/AC) and a simplified bi-linear stress-strain curve is used as shown in Table 1 [16]. Standard tension tests were conducted on the Al6061-T0 alloy to obtain the stress-strain curve which is determined to be $\sigma = 205\varepsilon^{0.2}$ (MPa) with Young's modulus of 69GPa and Poisson's ratio of 0.33.

2.4. RESULTS

2.4.1 FEA Validation of Young's modulus measurement

The comparative results of FEA and theoretical solutions were obtained. For both spherical and flat-end punch solution, the FEM results matched well with the analytical solutions except very near the contact boundary where the difference is noticeable. This is expected that, due to the plastic deformation, the region near the contact radius may deform irregularly [18]. Table 2 shows that the error for both flat-end and spherical models are all less than 5%.

Table 2. Error (%) of Young's modulus calculation

	Rigid Indenter	Deformable Indenter
Flat-end model	≤ 0.6%	≤ 3.3%
Spherical model	≤ 0.2%	≤ 1.7%

2.4.2 Fringe patterns of TIM system

To conduct indentation test using the TIM method, the gap between the indenter and specimen surface is filled with index matching fluid. The index changing rate of matching fluid is approximately -0.0004/°C. Without strict temperature control, initial fringe pattern is inevitable. As show in Figure 6, using TIM system, initial (no load) phase-shifted fringe patterns are shown in Figures 6(a) to 6(d). Figure 6(e) and 6(f) show phase map and unwrapped phase map. The outer denser irregular fringes are caused by the excessive optical glue. The white circle indicates the 2mm diameter indenter boundary.

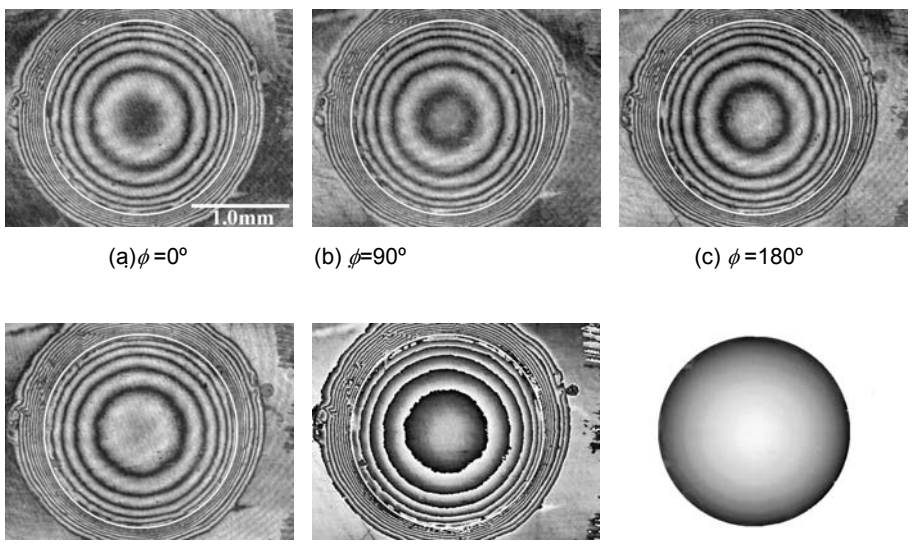

(a) ϕ =0º (b) ϕ=90º (c) ϕ =180º

(d) ϕ =270º (e) Phase map (f) Unwrapped phase

Figure 6. Typical TIM system initial fringe patterns

The initial fringe pattern affects the out-of-plane displacement measurement at each loading state. However, using phase-shifting technique, this initial fringe pattern can be easily subtracted. During loading, the specimen or indenter may be slightly tilted due to loading frame rigidity and specimen mounting. Thus the fringes are no longer symmetric, as typically shown in Figure 7. There are two methods to solve this problem. One is to adjust the reference mirror to restore the symmetry. Another is to use the axisymmetric feature of the indenter to automatically cancel out the inclination-induced

un-symmetric carrier fringes. In an actual indentation test, perfect alignment without any carrier fringes is unrealistic. Usually, one or half carrier fringe pattern may be present. Thus, it is also necessary to find a solution to correct this small carrier. As shown in Figure 7(b), it is found that the carrier effect can be automatically canceled out if the elastic recovery is averaged in 4 center-symmetric directions [15].

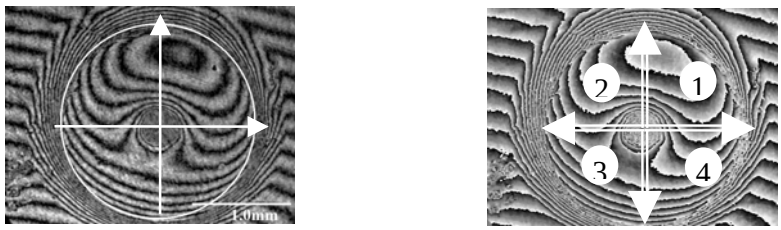

(a) Fringe pattern at loading status, with carrier (b) Phase map at loading status phase map

Figure 7. Inclination problem during loading-unloading

2.4.3 Elastic recovery and Young's modulus

Figure 8(a) shows typical loading fringe patterns, where outer white-lined circle denotes the indenter boundary. Figure 8(b) shows the corresponding phase map. Figure 8(c) is used to measure the contact radius. Figure 8(d) shows the typical unloading fringe patterns and Figure 8(e) shows the corresponding phase map. Figure 8(f) shows contact radius after unloading. No noticeable change in contact radius was found between loading and unloading. Phase map was first unwrapped to make it continuous, and then convert to out-of-plane displacement.

Figure 9 shows the loading and unloading fringe patterns, phase maps and contact radius images of one indentation for alloy Al6061-T0. The apparent carrier fringes were automatically canceled by averaging the elastic recovery in 4 center symmetric directions, e.g. Figure 7(b). The elastic recovery was calculated by subtracting loading and unloading displacement fields. Then Young's modulus was calculated using Eq.1. Table 3 shows error percentage of the Young's modulus calculation.

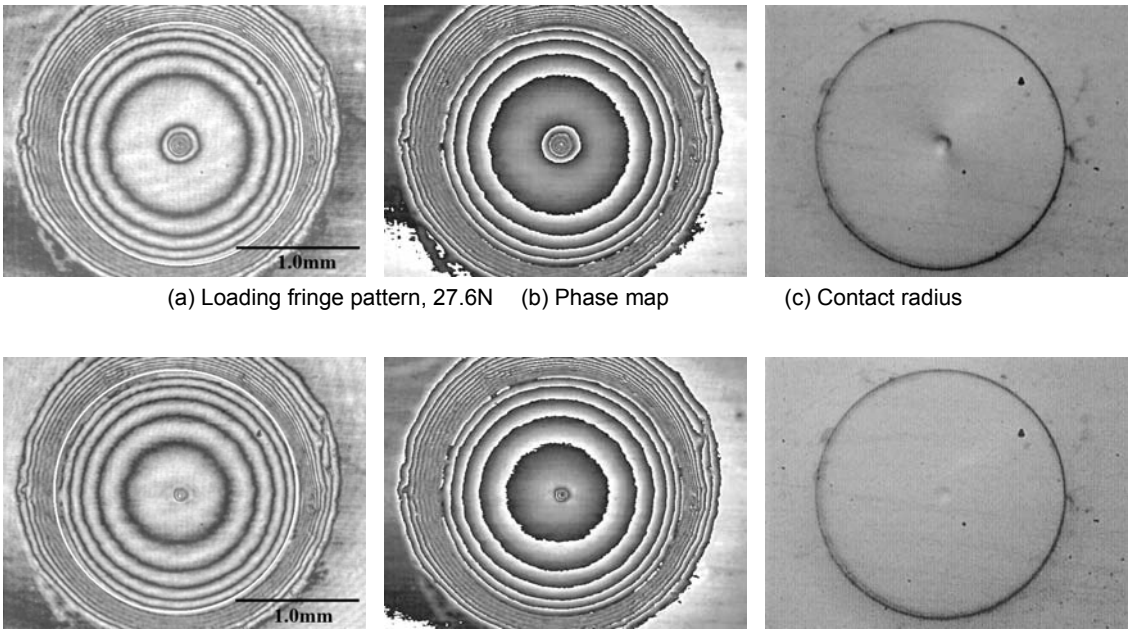

(a) Loading fringe pattern, 27.6N (b) Phase map (c) Contact radius

(d) Unloading fringe pattern (e) Phase map (f) Contact radius

Figure 8. Indentation of IN783 superalloy

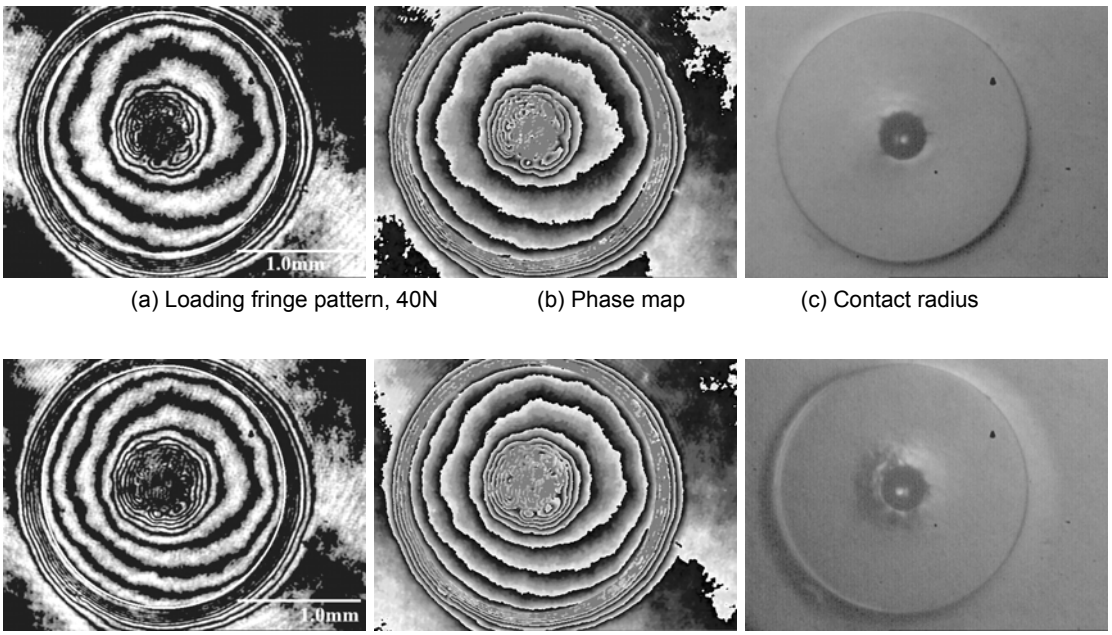

(a) Loading fringe pattern, 40N (b) Phase map (c) Contact radius

(d) Unloading fringe pattern (e) Phase map (f) Contact radius

Figure 9. Indentation of Al6061-T0 alloy

Table 3. Error(%) of the Young's modulus calculation

	IN783	Al 6061-T0
Flat-end model	≤ 6%	≤ 6%
Spherical model	≤ 5%	≤ 4%

2.4.4 Contact radius measurement for post-yielding stress-strain determination

After Young's modulus measurement, a sequence of monotonically increasing loads was applied at the same indented location. In-situ contact radius measurements were conducted to determine post-yielding stress-strain data using Tabor's empirical relation.

$$\varepsilon = 0.2\frac{d}{D} \qquad \sigma = \frac{P_m}{C} \qquad P_m = \frac{Load}{\pi a^2} \qquad (2)$$

where $d = 2a$ is the indent diameter and D is the indenter diameter, P_m is the mean pressure and C is the constraint factor.

For steel and copper alloy, C=2.8 was used by Tabor [13] with excellent correlation. However, in general, it was found to be strain hardening dependent. Taljat [19] suggested a more sophisticated analytical method to further derive the post-yielding behavior from the indentation stress-strain.

Figure 10 shows the in-situ contact radius measurements of IN783 superalloy with increasing loads. Due to its high strength, sapphire indenter was used to make indentation. Figure 11 shows in-situ contact radius measurements of Al6061-T0 alloy using BK7 indenter. The post-yielding stress-strain data determined from indentations are compared with the true stress-strain data respectively. They matched well using a proper constraint factor, i.e. C=2.9 for IN783 and C=2.8 for Al6061-T0. There is no apparent damage for the BK7 indenter for loading up to 300N, and for sapphire indenter, the load can be much larger without damaging the indenter.

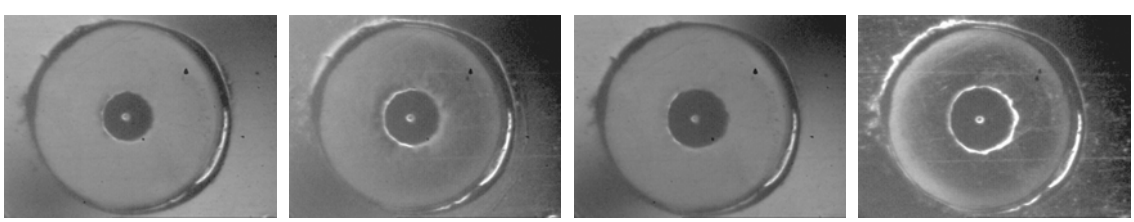

540N 689N 806N 904N

Figure 10. In-situ contact radius measurement of IN783 superalloy

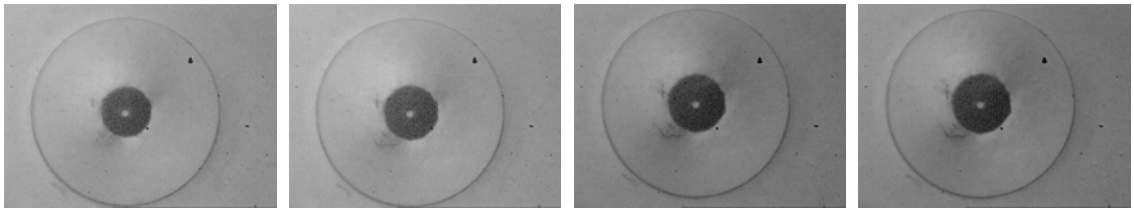

69.1N 84.0N 95.1N 99.6N

Figure 11. In-situ contact radius measurement of Al6061-T0 alloy

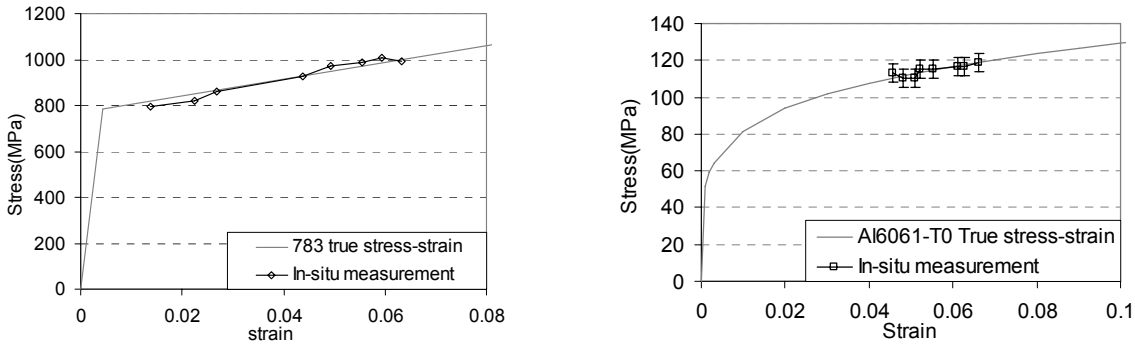

(a) IN783 (b) Al6061-T0

Figure 12. Post-yielding stress-strain data compared with true stress-strain curve

2.5 CONCLUSIONS AND DISCUSSIONS

An in-situ optical indentation measurement system, TIM method was developed. Using the TIM method, Young's modulus and post-yielding stress-strain behavior can be characterized through elastic recovery and in-situ contact radius measurement. Testing results of IN783 and Al6061-T0 showed good agreement with the known material properties. Finite element analyses also confirmed elastic recovery can be used to determine the Young's modulus using either flat-end punch or spherical indentation. Methods of automatically eliminating carrier fringe patterns was discussed and successfully used for both IN783 and Al6061-T0 tests, which makes TIM method suitable for fully automatic operation.

SUMMARY

Atomistic computational modeling and simulations on the influence of carbon and oxygen to grain boundary strength and interfacial fracture of molybdenum alloys were conducted. Using FP-LMTO techniques, we carried out a number of numerical simulations to probe the changes in electronic structures and chemical bonding properties due to the complex interactions among the impurity elements

and the hosting metal or metal-oxide interface. Interesting features in the charge density distribution plots were observed which may link to ductility enhancement.

Further computational investigation is suggested to study various impurity (in particular oxygen and carbon) grain boundaries segregation effects on the mechanical properties of molybdenum, and identify those that may help to improve the intergranular fracture resistance of molybdenum. The research will emphasize on an understanding of the fundamental mechanism at the atomic and electronic structure level, which will complement experimental result based on microstructural analysis at the micron-scale level.

An in-situ optical TIM indentation method was introduced. Finite element analyses confirmed elastic recovery can be used to determine the Young's modulus using either flat-end punch or spherical indentation. Using the TIM method, Young's modulus and post-yielding stress-strain behavior can be characterized through elastic recovery and in-situ contact radius measurement. Testing results of IN783 and Al6061-T0 showed good agreement with the known material properties. It is proposed to apply the TIM method for in-situ material mechanical property measurement as well as quick assessment of brittleness/ductility of alloys relevant to the Fossil Energy Materials Program**.**

ACKNOWLEDGMENTS

The work is sponsored by the Office of Fossil Energy, Advanced Research Materials (ARM) Program, U.S. Department of Energy, under contract DE-AC05-00OR22725 managed by UT-Battelle, LLC.

REFERENCE

1. A.K. Vasudevan and J. Petrovic, "A comparative overview of molybdenum silicide composites", Material Science and Engineering, A155, pp.1-17 (1992).
2. M.K. Meyer, A.J. Thom, and M. Akinc, "Compressive creep behavior of Mo_5Si_3 with the addition of boron", Intermetallics, 4, pp.273-281 (1996).
3. M.K. Meyer, M.J. Kramer, and M. Akinc, "Oxide scale formation and isothermal oxidation behavior of Mo-Si-B intermetallics at 600-1000°C", Intermetallics, 7, pp.153-162 (1999).

4. H. Choe, D. Chen, J. H. Schneibel, R. O. Ritchie, "Fracture and Fatigue-Crack Growth Behavior in Mo-12Si-8.5B Intermetallics at Ambient and Elevated Temperatures**,**" in Fatigue and Fracture Behavior of High Temperature Materials, P.K. Liaw, ed., TMS, Warrendale, PA, pp.17-24. (2001).
5. H. Choe, D. Chen, J.H. Schneibel, R.O. Ritchie, "Ambient to High Temperature Fracture Toughness and Fatigue-Crack Propagation Behavior in a Mo-12Si-8.5B (at.%) Intermetallic**,**" Intermetallics, 9, pp.319-329 (2001).
6. H. Choe, J. H. Schneibel, and R. O. Ritchie, "Fracture and Fatigue Properties of Mo-Mo_3Si-Mo_5SiB_2 Refractory Intermetallic Alloys at Ambient to Elevated Temperatures (25°C to 1300°C)**,**" Metallurgical and Materials Transactions, 34A (2), pp.225-239 (2003).
7. J. H. Schneibel, P. F. Tortorelli, M. J. Kramer, A. J. Thom, J. J. Kruzic, and R. O. Ritchie, "Optimization of Mo-Si-B Intermetallics," in Defect Properties and Related Phenomena in Intermetallic Alloys, E. P. George, M. J. Mills, H. Inui, G. Eggeler, eds., MRS Symposium Proceedings, vol. 753, Materials Research Society, Warrendale, PA, BB2.2.pp.1-6. (2003).
8. J. H. Schneibel, J. J. Kruzic, R. O. Ritchie, "Mo-Si-B Alloy Development," in Proceedings of the 17th Annual Conference on Fossil Energy Materials, (2003).
9. J. J. Kruzic, J. H. Schneibel, R. O. Ritchie,"Fracture and Fatigue Resistance of Mo-Si-B Alloys for Ultrahigh-Temperature Structural Applications," Scripta Materialia, 50 (4), pp.459-464 (2004).
10. D.L. Price, B.R. Cooper, and J.M. Wills, "Full-potential linear-muffin-tin-orbital study of brittle fracture in titanium carbide", Physical Review B, 46, pp.11368-11375 (1992).
11. D.L. Price, B.R. Cooper, and J.M. Wills, "Linear-muffin-tin-orbital calculation of TaC(001) surface relaxation", Physical Review B, 46, pp.15301-15310 (1993).
12. M.P. Brady, I.M. Anderson, M.L. Weaver, H.M. Meyer, L.R. Walker, M.K. Miller, D.J. Larson, I.G. Wright, V.K. Sikka, A.Rar, G.M. Pharr, J.R. Keiser, and C.A. Walls, "Nitrogen Impurity Gettering in Oxide Dispersion Ductilized Chromium,", Mater. Sci. Eng. A358, pp.243-254 (2003).
13. D. Tabor, The Hardness of Metals, Clarendon Press, Oxford, (1951).
14. K. L. Johnson, Contact Mechanics, Cambridge University Press, (1985).
15. Chuanyu Feng, Development of a Transparent Indenter Measurement system and Indentation Analysis for Material Mechanical Properties Evaluation, Dissertation, West Virginia University, (2005).
16. Special Metals Corporation, **http://www.specialmetals.com**.
17. B.S. –J, Kang, J. Skeen, K. Perry and Y.Y. Hung, Crack tip displacement measurements using automated phase shift moiré interferometry, 1997 SEM spring conference on experimental mechanics, pp311-312, Bellevue, WA, (1997).
18. John H. Underwood, Residual-stress measurement using surface displacements around an indentation, Experimental Mechanics, Vol. 13 No.9 pp 373-380, (1973).
19. B. Taljat, T. Zacharia, New analytical procedure to determine stress-strain curve from spherical indentation data, Int. J. Solids structures, Vol. 35, No. 33, pp. 4411-4426, (1998).